

Speed limits of the laser-induced phase transition in FeRh

M. Mattern,¹ J. Jarecki,¹ J. A. Arregi,² V. Uhlír,^{2,3} M. Rössle,⁴ and M. Bargheer^{1,4}

¹*Institut für Physik und Astronomie, Universität Potsdam, 14476 Potsdam, Germany*

²*CEITEC BUT, Brno University of Technology, 61200 Brno, Czech Republic*

³*Institute of Physical Engineering, Brno University of Technology, 61669 Brno, Czech Republic*

⁴*Helmholtz-Zentrum Berlin für Materialien und Energie GmbH,
Wilhelm-Conrad-Röntgen Campus, BESSY II, 12489 Berlin, Germany*

(Dated: March 1, 2024)

We use ultrafast x-ray diffraction (UXRD) and the polar time-resolved magneto-optical Kerr effect (tr-MOKE) to study the laser-induced metamagnetic phase transition in two FeRh films with thicknesses below and above the optical penetration depth. In the thin film, we identify an intrinsic timescale for the light-induced nucleation of ferromagnetic (FM) domains in the antiferromagnetic material of 8 ps that is substantially slower than the speed of sound. For the inhomogeneously excited thicker film, only the optically excited near-surface part transforms within 8 ps. For strong excitations we observe an additional slow rise of the FM phase, which we experimentally relate to a growth of the FM phase into the depth of the layer by comparing the transient magnetization in front- and backside excitation geometry. In the lower lying parts of the film, which are only excited via near-equilibrium heat transport, the FM phase emerges significantly slower than 8 ps after heating above the transition temperature.

First-order phase transitions are characterized by an abrupt change of structural, electronic or/and magnetic properties and a co-existence of multiple phases that introduces nucleation and domain growth to the kinetics of the phase transition [1–10].

The abrupt change of properties accompanying the emerging phase as a consequence of a fine interplay of spin, charge, orbital and lattice degrees of freedom [6, 11] predestine materials featuring first-order phase transitions for ultrafast laser control of functionalities [12]. In this context, the first-order antiferromagnetic to ferromagnetic (AFM-FM) phase transition of FeRh at 370 K attracted considerable attention in terms of ultrafast generation of ferromagnetic order [13, 14] that extends the more extensively studied ultrafast demagnetization [15, 16] and magnetization reversal [17–19].

The metamagnetic phase transition in FeRh is parameterized by the expansion of the unit cell [20], the change in the electronic band structure [21, 22] and the arising magnetization [23, 24], which each serve as order parameters for different aspects of the ultrafast laser-induced phase transition. Time-resolved photoelectron spectroscopy experiments reveal the formation of an electronic signature of the ferromagnetic state by a photo-induced change of the band structure on a sub-picosecond timescale [25]. X-ray magnetic circular dichroism [26, 27], magneto-optical Kerr effect (MOKE) [28] and double-pulse THz emission spectroscopy [29] report a subsequent formation of an in-plane magnetization on a 100 ps timescale. While the rise of a macroscopic magnetization is dominated by the slow coalescence and alignment of the nucleated domains in an external magnetic field [14, 29], the large FM lattice constant as structural order parameter is independent of the orientation of the arising magnetization [28]. Hence, ultrafast x-ray

diffraction (UXRD) directly accesses the nucleation and growth of FM domains that also determines the rise of the laser-induced magnetization within the first picoseconds [28, 29]. Previous UXRD studies report nucleation timescales ranging from 15 to 90 ps depending on the probing depth and fluence [28, 30]. Thus, the kinetics of the nucleation and growth of the laser-induced FM phase remains unclear and controversial.

Here, we use UXRD experiments on a homogeneously optically excited 12 nm thin FeRh film to identify an intrinsic fluence-, temperature- and field-independent 8 ps rise time of the structural order parameter. This nucleation of the FM phase is not limited by the speed of sound, which would require only 2.5 ps. For the inhomogeneously excited 44 nm thick film, we observe the same intrinsic 8 ps nucleation timescale and an additional delayed slow rise for high fluences when the deposited energy is sufficient to heat the lower lying parts beyond the transition temperature T_T by heat diffusion. This unlocks a growth of the FM phase into the depth of the film. Modeling the UXRD results shows that this growth driven by near-equilibrium heat transport is considerably slower than the 8 ps nucleation timescale after heating above T_T , indicating the crucial role of optically induced non-thermal states for the kinetics of the phase transition. The heat transport timescale is cross-checked by a buried tungsten detection layer, which measures the energy transmitted through FeRh. To complement the insights from the structural order parameter, we probe the subsequent formation of a macroscopic out-of-plane magnetization within 180 ps by polar tr-MOKE. When we excite the thick FeRh film from the backside, we find a considerable slower and fluence-dependent rise compared to frontside excitation, which experimentally verifies the slow out-of-plane growth of the FM phase.

The two samples are sketched in Fig. 1(a) and (b) and consist of a 12.6 nm thick FeRh film on MgO(001), and a 43.8 nm thick FeRh film embedded in a metallic heterostructure on MgO(001) consisting of a 2 nm Pt capping and a 8 nm W buffer layer. The thickness of the layers has been characterized via x-ray reflectivity (XRR) and the FeRh films were grown using magnetron sputtering from an equiatomic FeRh target [20]. Both FeRh films exhibit the first-order metamagnetic phase transition characterized by the temperature-dependent magnetization (solid lines) and average out-of-plane lattice constant d (symbols) displayed in Fig. 1(c) and (d). They were measured in thermal equilibrium via vibrating sample magnetometry (VSM) using a QuantumDesign VersaLab magnetometer and XRD performed at the KMC-3 XPP endstation at BESSY II [31], respectively.

The thin film exhibits a reduced mean transition temperature of $T_T = 365$ K in comparison to the thick film (375 K) and a residual FM phase fraction of around 20 % originating from interface effects [32–34]. This reduces the relative expansion associated with the AFM-FM phase transition from 0.6 % in the thick film to 0.48 % in the thin film. While the magnetization and lattice constant as order parameters of the temperature-induced phase transition nicely agree for the thick film, the inhomogeneity of the thin film results in a narrower hysteresis for the locally probed lattice constant in contrast to the global magnetization determined by VSM.

In the combined UXRD and tr-MOKE experiment, the FeRh layers are excited by p -polarized pump pulses with a central wavelength of 800 nm and 100 fs pulse duration that are incident under 50° with respect to the sample surface. Utilizing UXRD, we probe the transient out-of-plane strain response of the FeRh layers via reciprocal space mapping [35] of the FeRh(002) Bragg peak at a table-top laser-driven plasma x-ray source [36] providing 200 fs hard x-ray pulses with a photon energy of ≈ 8 keV. The Bragg peak position in reciprocal space is given by the average out-of-plane lattice constant d of the FeRh films via $q_z = 4\pi/d$. Therefore, the laser-induced peak shift accesses its change Δd determining the lattice strain $\eta_{\text{FeRh}} = \Delta d/d_0$ as the relative change with respect to its value d_0 before excitation.

Figure 2 displays the laser-induced strain response of both FeRh films and the buried W layer to a weak sub-threshold excitation that is not able to drive the AFM-FM phase transition [27, 28]. Thus, the strain response is the superposition of only two contributions: A quasi-static expansion due to heating and coherently driven propagating strain pulses (partially) reflected at the surface and interfaces. In the homogeneously excited 12 nm FeRh film (optical penetration depth $\lambda = 13$ nm), the laser excitation launches a strain pulse that is reflected at the surface and partially transmitted into the substrate. This results in a decaying oscillation with a period of $2L_{\text{FeRh}}/v_s$ determined by the layer thickness L_{FeRh} and

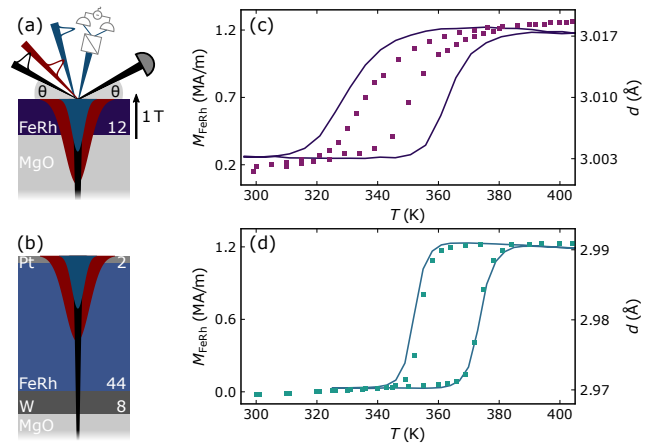


FIG. 1. **Characterization of FeRh films:** (a–b) Sketch of the sample structures containing a 12 nm and a 44 nm FeRh film, the excitation profile (red) and the probing profile of UXRD (black) and MOKE (blue). The combined UXRD and MOKE experiment is sketched in (a). Panels (c) and (d) compare the temperature-dependent magnetization (solid lines) with the out-of-plane lattice constant (symbols) parametrizing the AFM-FM phase transition in the thin and thick FeRh film, respectively.

the sound velocity v_s [38] that is superimposed with a decreasing quasi-static expansion due to heat transport into the substrate (see Fig. 2(a)). For the thick film sample, the bipolar strain pulse launched at the optically excited surface is partially reflected at the FeRh-W interface, which leads to a more complex shape of the oscillations in the FeRh strain response (see Fig. 2(b)). The compression of the W layer is caused by the leading part of the bipolar strain pulse generated in FeRh, and hence essentially senses the profile of optical energy deposition [38]. The W strain turns positive, when the expansive part of the strain pulse enters and the compressive part again exits the layer. The slowly rising expansion of W accesses the heat transport from FeRh into W on tens of picoseconds. These thermoelastic strain contributions scale linearly with the deposited energy [38].

In the following, we utilize this calibration of the thermoelastic strain response in the absence of a laser-induced AFM-FM phase transition to extract the transient FM volume fraction V_{FM} from the strain response to above-threshold excitations that additionally contains a strain signature from the forming FM phase. For this approach and to access the inhomogeneous spatio-temporal temperature profile within the 44 nm-thick FeRh film, we modeled the strain response by the modular PYTHON library UDKM1DSIM [39] utilizing literature values for the thermo-elastic properties stated in Tab. S1. We calculate the absorption profile and solve the one-dimensional heat diffusion equation determining the spatio-temporal temperature that determines the stress on the lattice [38]. By solving the linear one-dimensional elastic wave equa-

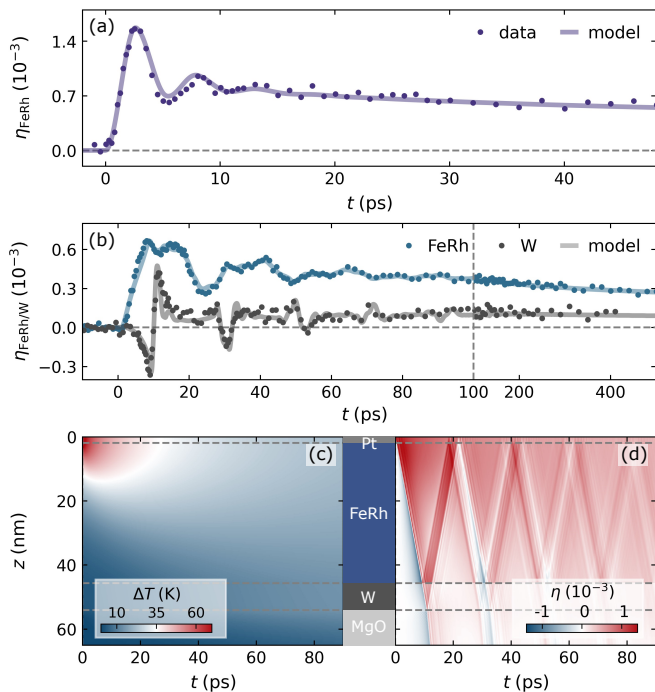


FIG. 2. **Thermoelastic strain response calibrated by UXR:** (a) Transient average strain of the 12 nm FeRh film (symbols) upon an excitation of $F_{st} = 0.5 \text{ mJ/cm}^2$. (b) Transient average strain response of the 44 nm FeRh and the W layer (symbols) for $F_{st} = 1.5 \text{ mJ/cm}^2$. The solid lines denote our strain model described in the text. The perfect agreement shown in (b) is a strong evidence for the correct modeling of the corresponding the spatio-temporal temperature increase $\Delta T(z, t)$ (c) and strain $\eta(z, t)$ (d).

tion for this stress we finally calculate the strain response [38] (see supplementary material S1 for a detailed description of the strain modeling). Figures 2(c) and (d) display the spatio-temporal strain η and temperature increase ΔT for $F_{st} = 1.6 \text{ mJ/cm}^2$, respectively. Averaging the strain $\eta(z, t)$ over a respective layer yields the layer-specific strain response measured in our UXR experiment. We find excellent agreement of the modeled strain response (solid lines) with the measurements in both samples. The excellent agreement with both the 44 nm FeRh and the buried W layer for a single set of parameters pinpoints the modeled spatio-temporal temperature shown in Fig. 2(c). The shape of the initial compression of W quantifies the absorption profile and its slowly rising expansion probes the heat propagated through the inhomogeneously excited FeRh layer [38].

Figure 3(a) displays the strain response of the 12 nm-thin FeRh film for various fluences below and above the threshold of the phase transition. The dashed line denotes the modeled thermoelastic strain scaled to 1.8 mJ/cm^2 , i.e. the hypothetical strain response without phase transition. The very large difference to the actual measurement (coloured area) highlights the signature of

the phase transition in the strain response. The strain measured in an external magnetic field of 1 T (squares) is identical to the response without an applied magnetic field (dots). This shows that the signature of the phase transition in the structural response is independent of the external magnetic field. We relate the additional strain contribution to $V_{FM}(t)$ by considering the expansion of 0.48 % for a complete phase transition in thermal equilibrium (see Fig. 1(c)). In addition, we considered the thermal expansion coefficient of the FM phase (see Tab. S1) and that the energy consumed by the latent heat 4.2 J/gK [40] at the transition temperature does not contribute to thermoelastic expansion. Figure 3(b) displays the extracted FM volume fraction $V_{FM}(t)$ that parameterizes the laser-driven phase transition. We observe that $V_{FM}(t)$ rises as a single exponential according to:

$$V_{FM}(t) = V_{FM}^* \cdot \left(1 - e^{-t/\tau}\right), \quad (1)$$

where V_{FM}^* denotes the final fraction of the film in the FM phase and τ is the rise time, independent of the fluence and the applied magnetic field. This model of V_{FM} has been discussed and successfully applied in a previous UXR study of FeRh [28] and assumes the nucleation of FM domains at independent sites according to Avrami [1]. We observe an intrinsic $\tau = 7.8 \pm 0.6 \text{ ps}$ timescale from the fit of all measurements in Fig. 3(b). This is clearly slower than the relaxation of the lattice: The propagation of strain pulses through the thin film at the speed of sound only takes the time $L_{FeRh}/v_s = 2.5 \text{ ps}$ (cf. Fig. 3(a)). We can therefore definitely exclude the widely accepted hypothesis that the sound velocity v_s sets the speed limit for the AFM-FM phase transition in FeRh [28, 29, 41]. Instead, the structural order parameter intrinsically responds on an 8 ps timescale to direct optical excitation. The transformed volume fraction V_{FM}^* increases with fluence and saturates at $F_{sat} = 2.1 \text{ mJ/cm}^2$, when the complete film is driven into the FM phase. Figure 3(b) shows that $F = 3.4 \text{ mJ/cm}^2$ yields the same V_{FM}^* , although the thermoelastic strain contributions grow (Fig. 3(a)).

We complement the insights of the UXR measurements by measuring the transient out-of-plane magnetization by polar MOKE in the very same experimental setup under identical excitation conditions. We applied a maximum out-of-plane magnetic field of 1 T provided by an electromagnet. The transient magnetization is extracted by the difference of the transient MOKE signal for opposite field-polarities. The 100 fs-long p -polarized probe pulse with a central wavelength of 400 nm is focussed through the pole of the magnet and is incident under less than 2° with respect to the sample normal.

The transient out-of-plane magnetization in Fig. 3(c) verifies this fluence dependence of V_{FM}^* . Up to the threshold fluence of $F_{th} = 0.6 \text{ mJ/cm}^2$ we observe no macroscopic magnetization at all and a fluence of 2.1 mJ/cm^2

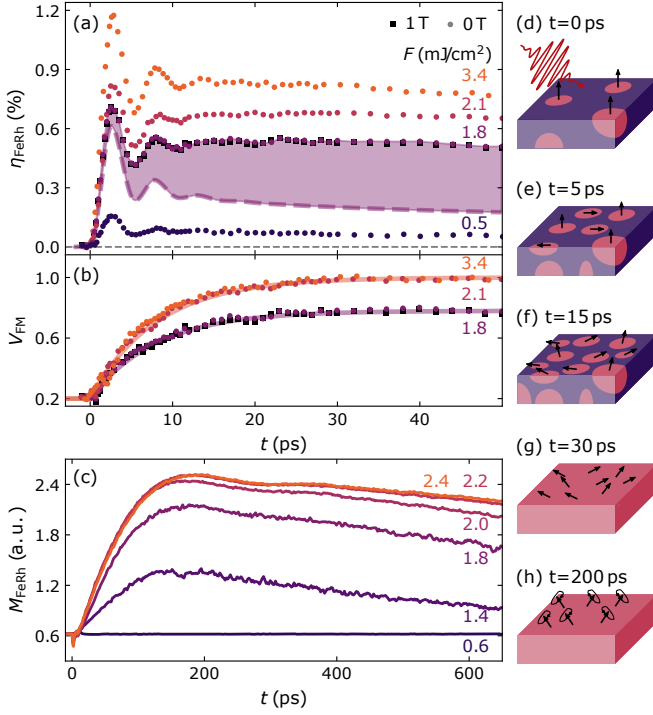


FIG. 3. **Intrinsic timescale of nucleation:** (a) Fluence-dependent strain response of the 12 nm thick FeRh film. The strain response for a field of 1 T (squares) matches the one without external field (dots). The dashed line is the modeled strain for 0.5 mJ/cm² scaled to 1.8 mJ/cm², i.e. the hypothetical response without phase transition. (b) Transient FM volume fraction V_{FM} extracted from the difference (coloured area) between measurement and modeled thermoelastic strain. (c) Fluence-dependent transient out-of-plane magnetization from polar MOKE. Field-dependent MOKE data are presented in Fig. S4 in the supplementary material. Panels (d–h) sketch the kinetics of the phase transition in regard of the structural order parameter (pink color) and the magnetization (arrows) in line with previous results [14, 28, 29, 43]. After the nucleation of FM domains the local magnetization precessionally tilts out-of-plane plane (g,h).

fully saturates the laser-induced magnetization. We observe a fluence-independent rise time with the maximum signal at 180 ps for 1 T, i.e. much slower than the nucleation of the FM domains. This slow formation of a macroscopic magnetization by the alignment of the local magnetization of the nucleated domains was reported previously [27–29]: The local magnetization initially lies in the sample plane along four equal directions determined by a cubic anisotropy of around 100 mT that represent the magnetic easy axes due to the shape anisotropy field of 1.38 T for thin FeRh films [28, 42]. For an in-plane magnetic field, a macroscopic in-plane magnetization is formed by field-driven coalescence of the FM domains via domain wall motion in agreement with the observed linear increase of the growth rate of the macroscopic magnetization with the field [29]. For the out-of-plane mag-

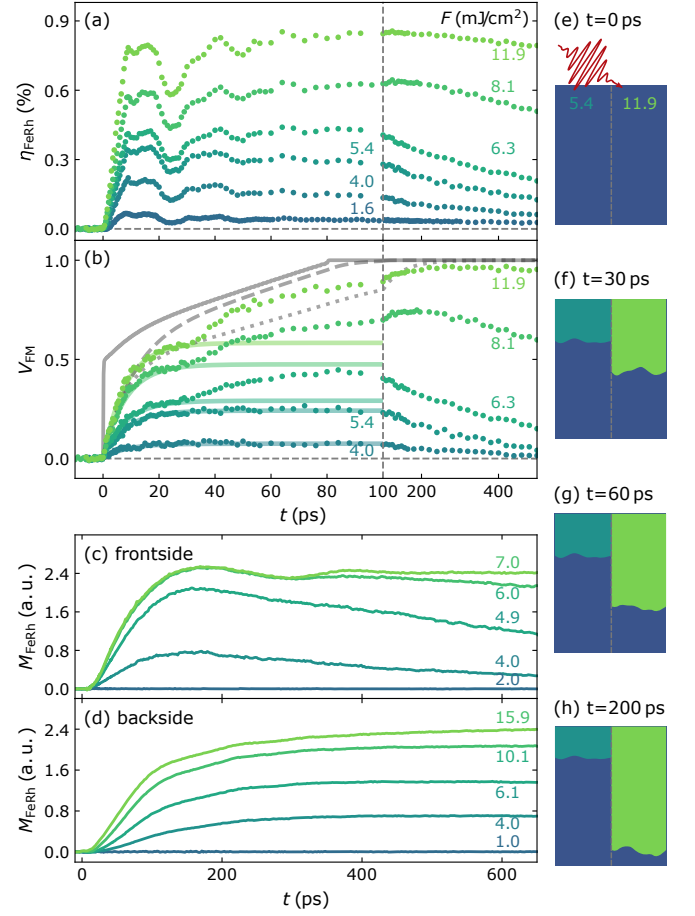


FIG. 4. **Kinetics of out-of-plane growth of the FM phase:** (a) Fluence-dependent field-free strain response of the 44 nm thick FeRh film. (b) Transient FM volume fraction derived analogously to the thin film by comparing the measured strain to a scaled sub-threshold strain model. (c,d) Fluence-dependent magnetization rise measured by polar MOKE with a magnetic field of 1 T in front- and backside excitation geometry, respectively. (e–h) Sketch of the out-of-plane growth of the FM phase indicated by the green area for 5.4 (left) and 11.9 mJ/cm² (right) that is induced by a fluence-dependent heating above T_{T} at the backside of the film via near-equilibrium heat transport.

netization, in contrast, we observe the maximum to be established faster for smaller out-of-plane fields (Fig. S4). This is consistent with precessionally tilting [14] the magnetization of the nucleated domains out of the sample plane. Figures 3(d–h) sketch the series of events.

These MOKE results upon direct optical excitation of the thin film serve as reference for the inhomogeneously excited thick film where the redistribution of energy within the layer by heat transport extends the dynamics of the phase transition. We utilize the finite probing depth of MOKE to gain insights into the out-of-plane evolution of the FM phase by comparing the rising magnetization at the sample surface for front- and backside excitation in Figs. 4(c and d). For frontside excitation,

we observe the same fluence-independent rise time as for the thin film in Fig. 3(c). In contrast, exciting through the substrate leads to a delayed and slower rise. Additionally, the rise time strongly depends on the fluence (see Fig. S3 for a comparison normalized to the maximum). The delayed and much slower rise for backside excitation is fluence-dependent, indicating a slow out-of-plane growth of V_{FM} via near-equilibrium heat transport that brings the upper part of the film above the transition temperature. However, the tr-MOKE measurements cannot quantify whether it is the heat transport or different kinetics of the phase transition in near-equilibrium that yield the increased timescale.

In order to determine the speed at which the FM phase nucleates and grows in the thick film, we again subtract the fluence-scaled strain response to a sub-threshold excitation F_{st} in Fig. 4(a) measured by UXRD from the strain measured above the threshold. The resulting transient FM volume fraction in Fig. 4(b) displays the change from a single exponential rise for low fluences to a two-step rise for high fluences ($> 6 \text{ mJ/cm}^2$). For all fluences V_{FM} rises according to Eq. (1) with the intrinsic 8 ps timescale already observed in the thin film during the first 30 ps (see solid colored lines in Fig. 4(b)). The amplitude of the additional contribution in the high fluence regime increases with the fluence. The maximum V_{FM} is reached at increasing delays up to 250 ps for the highest fluence, where the complete FeRh film is driven across the AFM-FM phase transition. Reaching the full transformation to the FM phase in Fig. 4(b) shows that for high fluences the temperature at the backside finally exceeds the transition temperature T_{T} , thus enabling the phase transition in near-equilibrium. This results in the two-step rise of V_{FM} for high fluences in contrast to a phase transition on the 8 ps timescale limited to the optically excited near-surface region for low fluences as sketched in Fig. 4(e-h). Note, that the laterally homogeneous growth of the FM phase into the depth, which follows the inhomogeneous optical excitation, differs from the dynamics observed for homogeneous equilibrium heating [2], where columns through the FeRh film are formed after the nucleation of FM domains at both interfaces before the in-plane domain growth.

To crosscheck our interpretation, we repeated the UXRD varying the initial sample temperature (cf. Fig. S2). At temperatures only slightly below T_{T} the laser excitation is sufficient to drive the phase transition in the not directly excited bottom part of FeRh, which results in a two-step rise of V_{FM} . At lower temperatures, the heating is insufficient and we observe only a rise on the 8 ps timescale. In this temperature-dependent experiment, we directly accessed V_{FM} by the transient relative amplitudes of the structural Bragg peaks of the AFM and FM phase that are separated in reciprocal space due to the excellent collimation of the x-ray beam at the KMC-3 XPP endstation at BESSY II [31]. This parameter-

free analysis also applied by Mariager and co-workers [28] serves as a crosscheck of our findings in Fig. 3 and 4. The slow growth of the FM phase into the depth unlocked by strong excitations explains the different timescales for different fluences and probing depth reported in previous UXRD experiments on inhomogeneously excited FeRh films [28, 30]. The exponential probing profile in grazing incidence geometry in previous experiments [28] may have masked the clear two-step behaviour in our experiments.

We obtain additional insights into the growth of the FM phase within the inhomogeneously excited FeRh layer from the modeled spatio-temporal temperature profile $T(z, t)$ in Fig. 2(c). From this analysis, we obtain the gray solid line in Fig. 4(b), which denotes the fraction of the film transiently heated above $T_{\text{T}} = 375 \text{ K}$ for an excitation of 11.9 mJ/cm^2 . This analysis shows that already within the first 30 ps a considerably large fraction and within 80 ps the complete film is heated above the transition temperature. This is much faster than the observed rise of V_{FM} within 250 ps and indicates that the growth of the FM phase does not simply follow the heating of the backside above T_{T} but exhibits intrinsic kinetics. If we assume the FM phase to locally rise with an 8 ps timescale as soon as the local temperature exceeds T_{T} , the modeled rise of V_{FM} (gray dashed line) is still significantly faster than in the measurement. Therefore, establishing the FM phase by only near-equilibrium heating must be considerably slower than the nucleation in the optically excited near-surface part of the film. The gray dotted line in Fig. 4(b) represents the combination of an 8 ps nucleation timescale for the optically heated unit cells and a second 50 ps timescale for the formation of the FM phase for unit cells heated above T_{T} by heat transport. This approach matches the delay when V_{FM}^* is reached and provides an estimation of the intrinsic timescale related to the phase transition driven by near-equilibrium heating via thermal electrons and phonons.

In summary, we discovered an intrinsic fluence-, temperature- and field-independent 8 ps timescale for locally establishing macroscopic properties of the FM phase in FeRh via nucleation of domains upon direct optical excitation. This timescale is not limited by the relaxation of the lattice with sound velocity as stated previously [28, 41] but represents intrinsic kinetics of the first-order phase transition. In the high fluence regime and for sample temperatures near the transition temperature, we additionally observe a delayed and slow growth of the FM phase into the depth of an inhomogeneously excited FeRh layer driven by near-equilibrium heat transport. This observation explains the different rise times of the structural order parameter in previous UXRD experiments [28, 30]. Our modeling reveals that the rise of the FM phase after heating above the transition temperature by near-equilibrium heat transport is substantially slower than nucleation driven by direct optical excitation.

This hints to the crucial role of modifying the electronic band structure within the first picosecond via photoexcited electrons[25] for the kinetics of the subsequent formation of the equilibrium FM phase.

We acknowledge the DFG for financial support via No. BA 2281/11-1 and Project-No. 328545488 – TRR 227, project A10. V. U. acknowledges the project CZ.02.01.01/00/22.008/0004594. Access to the Czech-NanoLab Research Infrastructure was supported by the MEYS CR (LM2023051). Beamtimes at the KMC-3 XPP endstation of the synchrotron radiation facility BESSY II at the Helmholtz Zentrum Berlin were required for thorough sample characterization and parameter-free crosscheck measurements.

-
- [1] M. Avrami, Kinetics of phase change. i general theory, *The Journal of chemical physics* **7**, 1103 (1939).
- [2] C. Gatel, B. Warot-Fonrose, N. Biziere, L. Rodríguez, D. Reyes, R. Cours, M. Castiella, and M.-J. Casanove, Inhomogeneous spatial distribution of the magnetic transition in an iron-rhodium thin film, *Nature Communications* **8**, 15703 (2017).
- [3] V. Uhlř, J. A. Arregi, and E. E. Fullerton, Colossal magnetic phase transition asymmetry in mesoscale ferri stripes, *Nature communications* **7**, 13113 (2016).
- [4] J. A. Arregi, F. Ringe, J. Hajduček, O. Gomonay, T. Molnár, J. Jaskowiec, and V. Uhlř, Magnetic-field-controlled growth of magnetoelastic phase domains in ferri, *Journal of Physics: Materials* **6**, 034003 (2023).
- [5] S. Roy, G. Perkins, M. Chattopadhyay, A. Nigam, K. Sokhey, P. Chaddah, A. Caplin, and L. Cohen, First order magnetic transition in doped ceFe 2 alloys: Phase coexistence and metastability, *Physical review letters* **92**, 147203 (2004).
- [6] S. De Jong, R. Kukreja, C. Trabant, N. Pontius, C. Chang, T. Kachel, M. Beye, F. Sorgenfrei, C. Back, B. Bräuer, *et al.*, Speed limit of the insulator–metal transition in magnetite, *Nature materials* **12**, 882 (2013).
- [7] F. Randi, I. Vergara, F. Novelli, M. Esposito, M. Dell’Angela, V. Brabers, P. Metcalf, R. Kukreja, H. A. Dürr, D. Fausti, *et al.*, Phase separation in the nonequilibrium verwey transition in magnetite, *Physical Review B* **93**, 054305 (2016).
- [8] M. M. Qazilbash, M. Brehm, B.-G. Chae, P.-C. Ho, G. O. Andreev, B.-J. Kim, S. J. Yun, A. Balatsky, M. Maple, F. Keilmann, *et al.*, Mott transition in vo2 revealed by infrared spectroscopy and nano-imaging, *Science* **318**, 1750 (2007).
- [9] C. Baldasseroni, C. Bordel, A. Gray, A. Kaiser, F. Kronast, J. Herrero-Albillos, C. Schneider, C. Fadley, and F. Hellman, Temperature-driven nucleation of ferromagnetic domains in ferri thin films, *Applied Physics Letters* **100**, 262401 (2012).
- [10] D. J. Keavney, Y. Choi, M. V. Holt, V. Uhlř, D. Arena, E. E. Fullerton, P. J. Ryan, and J.-W. Kim, Phase coexistence and kinetic arrest in the magnetostructural transition of the ordered alloy ferri, *Scientific reports* **8**, 1778 (2018).
- [11] S. Polesya, S. Mankovsky, D. Ködderitzsch, J. Minár, and H. Ebert, Finite-temperature magnetism of ferri compounds, *Physical Review B* **93**, 024423 (2016).
- [12] D. Wegkamp, M. Herzog, L. Xian, M. Gatti, P. Cudazzo, C. L. McGahan, R. E. Marvel, R. F. Haglund Jr, A. Rubio, M. Wolf, *et al.*, Instantaneous band gap collapse in photoexcited monoclinic vo 2 due to photocarrier doping, *Physical review letters* **113**, 216401 (2014).
- [13] G. Ju, J. Hohlfeld, B. Bergman, R. J. van de Veerdonk, O. N. Mryasov, J.-Y. Kim, X. Wu, D. Weller, and B. Koopmans, Ultrafast generation of ferromagnetic order via a laser-induced phase transformation in ferri thin films, *Physical review letters* **93**, 197403 (2004).
- [14] B. Bergman, G. Ju, J. Hohlfeld, R. J. van de Veerdonk, J.-Y. Kim, X. Wu, D. Weller, and B. Koopmans, Identifying growth mechanisms for laser-induced magnetization in ferri, *Physical Review B* **73**, 060407 (2006).
- [15] E. Beaurepaire, J.-C. Merle, A. Daunois, and J.-Y. Bigot, Ultrafast spin dynamics in ferromagnetic nickel, *Physical review letters* **76**, 4250 (1996).
- [16] A. Kirilyuk, A. V. Kimel, and T. Rasing, Ultrafast optical manipulation of magnetic order, *Reviews of Modern Physics* **82**, 2731 (2010).
- [17] C. D. Stanciu, F. Hansteen, A. V. Kimel, A. Kirilyuk, A. Tsukamoto, A. Itoh, and T. Rasing, All-optical magnetic recording with circularly polarized light, *Physical review letters* **99**, 047601 (2007).
- [18] I. Radu, K. Vahaplar, C. Stamm, T. Kachel, N. Pontius, H. Dürr, T. Ostler, J. Barker, R. Evans, R. Chantrell, *et al.*, Transient ferromagnetic-like state mediating ultrafast reversal of antiferromagnetically coupled spins, *Nature* **472**, 205 (2011).
- [19] Q. Remy, J. Hohlfeld, M. Vergès, Y. Le Guen, J. Gorchon, G. Malinowski, S. Mangin, and M. Hehn, Accelerating ultrafast magnetization reversal by non-local spin transfer, *Nature Communications* **14**, 445 (2023).
- [20] J. A. Arregi, O. Caha, and V. Uhlř, Evolution of strain across the magnetostructural phase transition in epitaxial ferri films on different substrates, *Physical Review B* **101**, 174413 (2020).
- [21] A. Gray, D. Cooke, P. Krüger, C. Bordel, A. Kaiser, S. Moyerman, E. Fullerton, S. Ueda, Y. Yamashita, A. Gloskovskii, *et al.*, Electronic structure changes across the metamagnetic transition in ferri via hard x-ray photoemission, *Physical review letters* **108**, 257208 (2012).
- [22] F. Pressacco, V. Uhlř, M. Gatti, A. Nicolaou, A. Bendounan, J. A. Arregi, S. K. Patel, E. E. Fullerton, D. Krizmancic, and F. Sirotti, Laser induced phase transition in epitaxial ferri layers studied by pump-probe valence band photoemission, *Structural Dynamics* **5**, 034501 (2018).
- [23] S. Maat, J.-U. Thiele, and E. E. Fullerton, Temperature and field hysteresis of the antiferromagnetic-to-ferromagnetic phase transition in epitaxial ferri films, *Physical Review B* **72**, 214432 (2005).
- [24] C. Stamm, J.-U. Thiele, T. Kachel, I. Radu, P. Ramm, M. Kosuth, J. Minár, H. Ebert, H. Dürr, W. Eberhardt, *et al.*, Antiferromagnetic-ferromagnetic phase transition in ferri probed by x-ray magnetic circular dichroism, *Physical Review B* **77**, 184401 (2008).
- [25] F. Pressacco, D. Sangalli, V. Uhlř, D. Kutnyakhov, J. A. Arregi, S. Y. Agustsson, G. Brenner, H. Redlin, M. Heber, D. Vasilyev, *et al.*, Subpicosecond metamagnetic phase transition in ferri driven by non-equilibrium

- electron dynamics, *Nature Communications* **12**, 5088 (2021).
- [26] A. Ünal, A. Parabas, A. Arora, J. Ehrler, C. Barton, S. Valencia, R. Bali, T. Thomson, F. Yildiz, and F. Kronast, Laser-driven formation of transient local ferromagnetism in ferh thin films, *Ultramicroscopy* **183**, 104 (2017).
- [27] I. Radu, C. Stamm, N. Pontius, T. Kachel, P. Ramm, J.-U. Thiele, H. Dürr, and C. Back, Laser-induced generation and quenching of magnetization on ferh studied with time-resolved x-ray magnetic circular dichroism, *Physical Review B* **81**, 104415 (2010).
- [28] S. O. Mariager, F. Pressacco, G. Ingold, A. Caviezol, E. Möhr-Vorobeva, P. Beaud, S. Johnson, C. Milne, E. Mancini, S. Moyerman, *et al.*, Structural and magnetic dynamics of a laser induced phase transition in ferh, *Physical Review Letters* **108**, 087201 (2012).
- [29] G. Li, R. Medapalli, J. Mentink, R. Mikhaylovskiy, T. Blank, S. Patel, A. Zvezdin, T. Rasing, E. Fullerton, and A. Kimel, Ultrafast kinetics of the antiferromagnetic-ferromagnetic phase transition in ferh, *Nature Communications* **13**, 2998 (2022).
- [30] F. Quirin, M. Vattilana, U. Shymanovich, A.-E. El-Kamhawy, A. Tarasevitch, J. Hohlfeld, D. von der Linde, and K. Sokolowski-Tinten, Structural dynamics in ferh during a laser-induced metamagnetic phase transition, *Physical Review B* **85**, 020103 (2012).
- [31] M. Rössle, W. Leitenberger, M. Reinhardt, A. Koç, J. Pudell, C. Kwamen, and M. Bargheer, The time-resolved hard x-ray diffraction endstation kmc-3 xpp at bessy ii, *Journal of Synchrotron Radiation* **28**, 948 (2021).
- [32] F. Pressacco, V. Uhlř, M. Gatti, A. Bendouan, E. E. Fullerton, and F. Sirrotti, Stable room-temperature ferromagnetic phase at the ferh (100) surface, *Scientific reports* **6**, 22383 (2016).
- [33] R. Fan, C. J. Kinane, T. Charlton, R. Dorner, M. Ali, M. De Vries, R. M. Brydson, C. H. Marrows, B. J. Hickey, D. A. Arena, *et al.*, Ferromagnetism at the interfaces of antiferromagnetic ferh epilayers, *Physical Review B* **82**, 184418 (2010).
- [34] X. Chen, J. Feng, Z. Wang, J. Zhang, X. Zhong, C. Song, L. Jin, B. Zhang, F. Li, M. Jiang, *et al.*, Tunneling anisotropic magnetoresistance driven by magnetic phase transition, *Nature Communications* **8**, 449 (2017).
- [35] D. Schick, R. Shayduk, A. Bojahr, M. Herzog, C. v. Korff Schmising, P. Gaal, and M. Bargheer, Ultrafast reciprocal-space mapping with a convergent beam, *Journal of Applied Crystallography* **46**, 1372 (2013).
- [36] D. Schick, A. Bojahr, M. Herzog, C. v. K. Schmising, R. Shayduk, W. Leitenberger, P. Gaal, and M. Bargheer, Normalization schemes for ultrafast x-ray diffraction using a table-top laser-driven plasma source, *Review of Scientific Instruments* **83**, 025104 (2012).
- [37] L. Willig, A. von Reppert, M. Deb, F. Ganss, O. Hellwig, and M. Bargheer, Finite-size effects in ultrafast remagnetization dynamics of fept, *Physical Review B* **100**, 224408 (2019).
- [38] M. Mattern, A. von Reppert, S. P. Zeuschner, M. Herzog, J.-E. Pudell, and M. Bargheer, Concepts and use cases for picosecond ultrasonics with x-rays, *Photoacoustics* **31**, 100503 (2023).
- [39] D. Schick, udkm1dsim—a python toolbox for simulating 1d ultrafast dynamics in condensed matter, *Computer Physics Communications* **266**, 108031 (2021).
- [40] M. Richardson, D. Melville, and J. Ricodeau, Specific heat measurements on an fe rh alloy, *Physics Letters A* **46**, 153 (1973).
- [41] K. Kang, H. Omura, S. Inoue, D. Yesudas, author O. Lee, author K. J. Lee, author H. W. Lee, T. Taniyama, and G. M. Choi, Spin current driven by ultrafast magnetization of FeRh, *Nature communications* **14**, 3619 (2023).
- [42] J. Cao, N. T. Nam, S. Inoue, H. Y. Y. Ko, N. N. Phuoc, and T. Suzuki, Magnetization behaviors for ferh single crystal thin films, *Journal of Applied Physics* **103**, 07F501 (2008).
- [43] N. Agarwal, Ultrafast dynamics of electronic structure and domain nucleation during photo-induced phase transition in FeRh, Ph.D. thesis, Staats-und Universitätsbibliothek Hamburg Carl von Ossietzky (2021).

Supplementary material to: Speed limits of the laser-induced phase transition in FeRh

M. Mattern,¹ J. Jarecki,¹ J. A. Arregi,² V. Uhlir,^{2,3} M. Rössle,⁴ and M. Bargheer^{1,4}

¹*Institut für Physik und Astronomie, Universität Potsdam, 14476 Potsdam, Germany*

²*CEITEC BUT, Brno University of Technology, 61200 Brno, Czech Republic*

³*Institute of Physical Engineering, Brno University of Technology, 61200 Brno, Czech Republic*

⁴*Helmholtz-Zentrum Berlin für Materialien und Energie GmbH,
Wilhelm-Conrad-Röntgen Campus, BESSY II, 12489 Berlin, Germany*

(Dated: March 1, 2024)

S1. MODELLING THE THERMOELASTIC STRAIN RESPONSE

In this section, we describe the procedure of modeling the transient strain response by using the modular PYTHON library UDKM1DSIM [1] and the layer-specific thermo-elastic parameters given in Tab. S1. In general, the UDKM1DSIM library captures the entire series of events in ultrafast x-ray diffraction (UXRD) experiments from the optically deposited energy density to the calculation of a Bragg peak shift via dynamical x-ray diffraction theory.

In our model approach, we do not individually treat electron and phonon degrees of freedom within the framework of a two-temperature model (2TM) since the literature does not provide separate values for the heat conductivity of electrons and phonons, their coupling and the electronic contribution to the thermal expansion in FeRh. Instead, our model only contains a single temperature that corresponds to the phonon temperature after electron-phonon equilibration in a 2TM. The initial temperature profile within the samples is determined by the optical penetration depth λ and the macroscopic heat capacity C_{ph} . The subsequent equilibration of the temperature across the metallic stack and the cooling towards the substrate determines the spatio-temporal temperature increase $\Delta T(z, t)$ by solving the diffusion equation accounting for the layer-specific heat capacities C_{ph} and thermal conductivities κ . The temperature increase determines the laser-induced stress $\sigma^{\text{ext}}(t) = c_{3333} \cdot \alpha_{\perp}^{\text{uf}} \cdot \Delta T(t)$ on ultrafast (uf) timescales via the expansion coefficient $\alpha_{\perp}^{\text{uf}}$ that accounts for the exclusive out-of-plane strain response of the metallic films and is calculated by $\alpha_{\perp}^{\text{uf}} = (1 + \frac{c_{1133} + c_{2233}}{c_{3333}}) \cdot \alpha$ considering the isotropic expansion coefficient α of bulk specimen [21]. The stress $\sigma^{\text{ext}}(t)$ drives the spatio-temporal strain response $\eta(z, t)$ as a superposition of a quasi-static expansion and coherently driven

	Pt	FeRh	W	MgO
unit cell orientation	(111)	(001)	(001)	(001)
number of simulated unit cells				
thin film	-	42 (12.6 nm)	-	substrate
thick film	8 (1.8 nm)	146 (43.8 nm)	28 (8.9 nm)	substrate
density ρ (g cm ⁻³)	21.45	9.93	19.25	3.58
elastic constants (GPa)	from [2]	from [3]	from [4]	from [5]
c_{3333}	386	285	523	289.3
c_{1133}	232	136	204	87.7
c_{2233}	232	136	204	87.7
out-of-plane sound velocity v_s (nm ps ⁻¹)	4.24	<u>5.00</u> (5.31)	5.21	9.12
lin. therm. expansion α (10 ⁻⁶ K ⁻¹)	8.9 [6]	9.7 (AFM) [7] 6.0 (FM) [7]	4.6 [6]	10.5 [8]
lin. therm. expansion $\alpha_{\perp}^{\text{uf}}$ (10 ⁻⁶ K ⁻¹)	19.6	19.6 (AFM) 12.4 (FM)	8.2	16.9
Grüneisen parameter of electrons Γ_{el}	1.4 [9]	<u>1.4</u>	<u>1.4</u>	-
Grüneisen parameter of phonons Γ_{ph}	2.6	1.7	1.6	1.7
electron-phonon coupling time $\tau_{\text{el-ph}}$ (ps)	0.4 [10]	<u>0.6</u>	0.6 [11]	-
heat capacity C_{ph} (J kg ⁻¹ K ⁻¹)	133 [12]	350 [13]	132 [14]	928 [15]
heat conductivity κ (W m ⁻¹ K ⁻¹)				
thin film	-	50 [16]	-	<u>20</u> (50 [17])
thick film	71 [18]	<u>25</u> (50 [16])	170 [19]	<u>20</u> (50 [17])
optical penetration depth λ (nm)				
thin film	-	multilayer [20]	-	inf
thick film	<u>13</u>	<u>13</u>	<u>8</u>	inf

TABLE S1. Thermo-elastic parameters of Pt, FeRh, W and the MgO substrate taken from the literature. Underlined values are optimized in the model to match the observed results. If literature values are available they are provided in parentheses.

propagating strain pulses determined by numerically solving the one-dimensional inhomogeneous elastic wave equation. Finally, the UDKM1DSIM library calculates Bragg peaks for each layer considering $\eta(z, t)$ via dynamical x-ray diffraction theory. Their transient shift is compared to the UXRD measurements.

The values used for the layer-specific thermo-elastic parameters involved in the model process mainly taken from the literature are stated in Tab. S1. Adjusted values are underlined in the table. In addition to the sequence described above, we include a finite stress rise time. In a one-temperature model this corresponds to a phenomenological electron-phonon coupling time $\tau_{\text{el-ph}}$, which mimics the solution of a 2TM. The different electronic and phononic Grüneisen parameters (Γ_{el} and Γ_{ph}) parametrize the efficiency of stress generation by energy deposition to the respective degree of freedom. Thus, we re-scale the temperature (energy) increase calculated from the heat diffusion equation by $\left(1 - \frac{\Gamma_{\text{ph}} - \Gamma_{\text{el}}}{\Gamma_{\text{ph}}}\right) \cdot e^{-t/\tau_{\text{el-ph}}}$ describing the corresponding stress rise. The phononic Grüneisen parameters are calculated from the thermal expansion via $\Gamma_{\text{ph}} = \alpha_{\perp}^{\text{uf}} \frac{c_{3333}}{C_{\text{ph}} \cdot \rho}$ and the electronic Grüneisen parameters are taken from the literature or optimized to match the shape and amplitude of the propagating strain pulses. The electron-phonon coupling timescale $\tau_{\text{el-ph}}$ in FeRh is estimated from transient reflectivity measurements. Furthermore, we determine the optical penetration depth of the thick sample by matching the shape of the strain pulse, especially the shape of the rapidly rising compression of the W buffer layer. In contrast, in the thin film we use a transfer-matrix formalism to calculate the absorption in terms of a multilayer model using literature values for the complex refractive index of FeRh [20] and MgO. To match the slow cooling of the optically excited FeRh layer towards W and the MgO substrate in Fig. 2, we reduce the heat conductivity of the FeRh film. We find the same quality of agreement with the data if we take the literature value for the heat conductivity in FeRh but reduce the heat conductivity of the first unit cell of W to 2 W/Km to model a large interface resistance. Under this assumption, the equilibration of the temperature within the FeRh layer would be even faster. This equally well supports the conclusion in the main text that the domain growth is considerably delayed with respect to the heating above T_T .

S2. TEMPERATURE-DEPENDENT LASER-INDUCED AFM-FM PHASE TRANSITION

In this section, we present the dependence of the laser-induced FM volume fraction on the initial sample temperature of the 44 nm-thick FeRh film that complements the fluence-dependent study in the main text and verifies the approach of extracting V_{FM} in the main text by similar findings for a parameter-free more direct approach of extracting V_{FM} following [23].

This experiment was performed at the KMC-3 XPP endstation of BESSY II in the low-alpha operation mode [24] with an x-ray pulse of 17 ps full-width half-maximum (FWHM) duration. Its parallel and monochromatic x-ray beam in contrast to the convergent beam at the plasma x-ray source [25, 26] enables the separation of the FM and AFM Bragg peaks in reciprocal space. The FM and AFM Bragg peaks represent the increase of the lattice constant across the metamagnetic phase transition. Their integrated intensities serve as a quantitative measure of the respective volume fraction of both phases co-existing during the laser-driven phase transition. The clear separation of the peaks in the synchrotron experiment enables a parameter-free determination of the transient FM volume fraction, and hence a measure of the phase transition kinetics without parametrizing the temperature-dependent thermal expansion as in the main text.

Figure S1(a) and (b) display the transient intensity distribution along the reciprocal q_z coordinate (symbols) encoding the out-of-plane lattice constant d via $q_z = 4\pi/d$ at 23 ps and 118 ps after excitation with a 600 fs laser pulse with a central wavelength of 1028 nm. The modeled intensity distribution (solid grey line) is the superposition of the AFM Bragg peak (blue) and the FM Bragg peak (green) at a larger lattice constant that emerges upon laser-excitation. Finally, the intensity distribution at each pump-probe delay yields V_{FM} by the integrated intensity of the FM Bragg peak with respect to the total diffracted intensity [23]. Figure S1(c) displays the transient V_{FM} at different initial sample temperatures ranging from 210 K to 330 K close to the transition temperature with a time-resolution of ≈ 15 ps given by the full-width half maximum of the x-ray pulse. We observe a similar behavior with increasing temperature as for increasing fluence in the main text. While the excitation well below the transition temperature only induces nucleation of FM domains on an 8 ps timescale, increasing the initial sample temperature enables the energy redistribution via heat transport to heat above the transition temperature which causes a growth of the nucleated FM domains into the depth of the film. As for high fluences, this results in a two-step rise of V_{FM} that becomes more dominant when approaching the transition temperature. The observation of a two-step rise of the FM volume fraction and a nice match of the first rise by an 8 ps timescale considering the temporal resolution of the experiment (solid lines in Fig. S1(c)) for the parameter free-extraction of V_{FM} following the approach of Mariager and co-workers [23] demonstrates the validity of the approach of extracting V_{FM} in the main text.

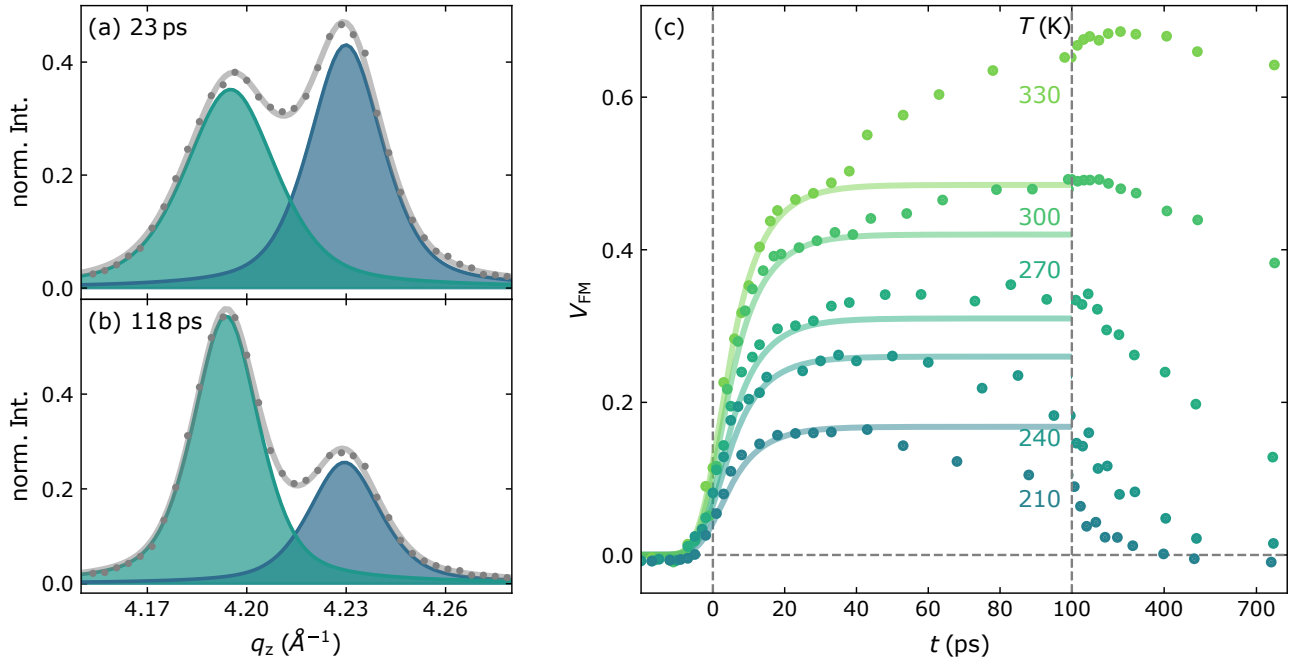


FIG. S1. **Two-step rise of FM volume fraction for excitation slightly below the transition temperature:** Transient rocking curve (grey) at 23 ps (a) and 118 ps (b) for an excitation of 6.5 mJ/cm^2 at 330 K separated into the Bragg peaks of the FM (green) and AFM phase (blue). In general, the integral of the Bragg peak is proportional to the fraction of the probed volume exhibiting the respective lattice structure. Therefore, the ratio of the integrated FM and AFM Bragg peak determines the transient FM volume fraction V_{FM} following the approach of Mariager and co-workers [23] for different initial sample temperatures in panel (c). The solid lines denote an exponential rise on an 8 ps timescale convoluted with a Gaussian of 17 ps FWHM representing the utilized x-ray pulse.

S3. FLUENCE-DEPENDENT MAGNETIZATION RISE FOR FRONT- AND BACKSIDE EXCITATION

Figure S2 presents the transient magnetization of the thick FeRh film from Fig. 3 in the main text normalized to its maximum. This representation for front- (a) and backside (b) excitation highlights the fluence dependence of the rise of the magnetization indicating the underlying kinetics of the AFM-FM phase transition. As a reference we additionally include the rise of the magnetization of the thin film as solid grey line. In frontside excitation geometry, the rise of the magnetization is independent from the fluence and in quantitative agreement with the behaviour of the thin film indicating optically induced nucleation in the near surface region of the thick FeRh film. In contrast, the rise of the magnetization at the sample surface after backside excitation becomes strongly fluence dependent and slows down with decreasing fluence. In addition, the magnetization rise is considerably slower than in the thin film and slightly delayed even for the highest fluence indicating the intrinsic kinetics of the domain growth driven by near-equilibrium heat transport. With increasing fluence less redistribution of the optically deposited energy density is required to heat the near-surface region above the transition temperature, which speeds up the formation of the FM phase.

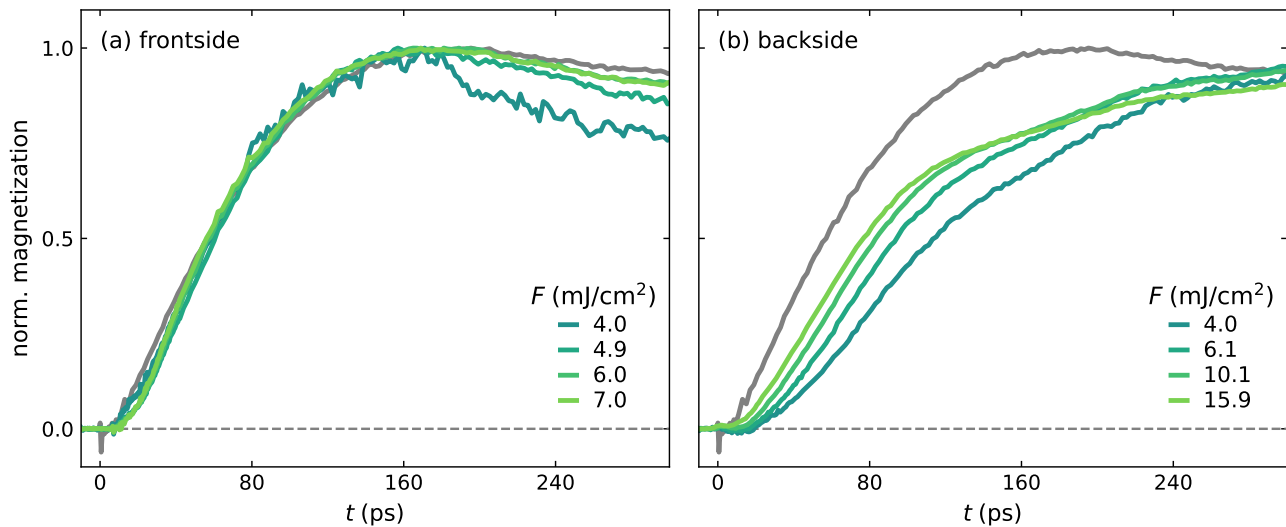


FIG. S2. **Fluence-dependent magnetization rise for front- and backside excitation:** Transient magnetization of the thick FeRh film from the main text normalized to the maximum in front- (a) and backside (b) excitation geometry for various fluences. The grey solid line denotes the rise of the normalized magnetization in the thin FeRh film. This representation highlights the fluence-independent rise for frontside excitation in quantitative agreement with the thin film and the decreasing speed of magnetization rise with decreasing fluence for backside excitation that is delayed in respect to the thin film dynamics originating from optically induced nucleation.

S4. FIELD-DEPENDENT MAGNETIZATION RISE

Figure S3 displays the laser-induced out-of-plane magnetization as function of the external magnetic field for both samples. These results extend the discussion in the main text and demonstrate a field-dependent frequency of the heavily damped precession and a field-dependent rise of the magnetization highlighted by the behaviour within the first 200 ps in panels (b) and (d). Independent from the external magnetic field we observe a latency of the rise of the magnetization of around 10 ps in agreement with previous work [27]. At high magnetic fields the larger maximum out-of-plane magnetization is reached later. The stronger external out-of-plane field tilts the effective field and hence the final direction of the magnetization further out of plane. Therefore, it takes longer to establish the maximum magnetization via the precessional motion of the magnetization. This observation for an out-of-plane magnetic field conceptually differs from the faster rise of an in-plane magnetization with increasing strength of the in-plane magnetic field due to domain wall motion in previous experiments [23, 27].

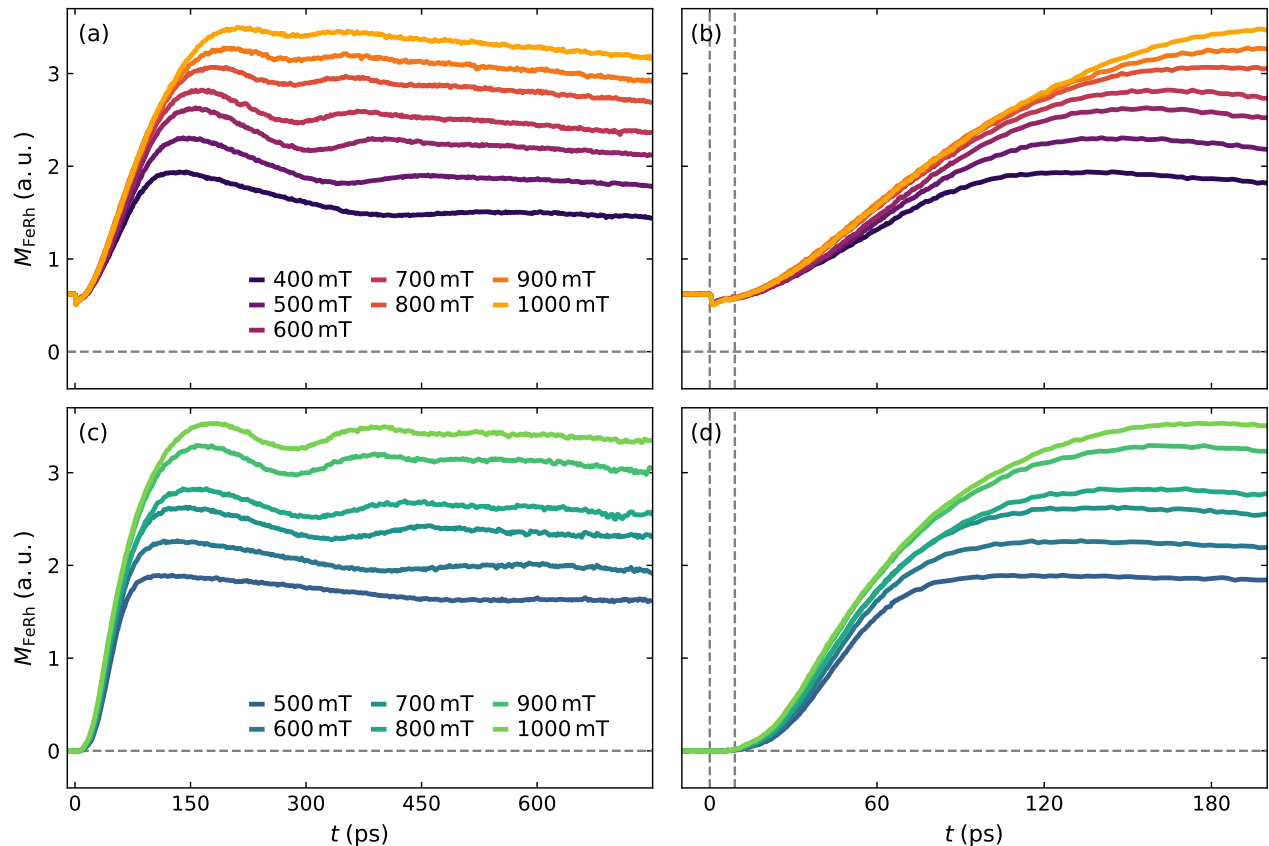


FIG. S3. **Field-dependent magnetization rise of both FeRh films:** Transient out-of-plane magnetization as function of the external magnetic field strength of the thin (a) and thick FeRh film (c). Panels (b) and (d) display the respective rise of the magnetization within the first 200 ps upon laser excitation. The vertical grey dashed lines indicate a field-independent latency in the rise of the out-of-plane magnetization of around 10 ps in agreement with previous work [27]. With increasing external magnetic field we observe a faster rise but a later establishing of the maximum out-of-plane magnetization that is not saturated up to 1 T due to a dominating shape anisotropy of 1.38 T given by the magnetization of FeRh [28].

-
- [1] D. Schick, udkm1dsim—a python toolbox for simulating 1d ultrafast dynamics in condensed matter, *Computer Physics Communications* **266**, 108031 (2021).
 - [2] R. MacFarlane, J. Rayne, and C. Jones, Temperature dependence of elastic moduli of iridium, *Physics Letters* **20**, 234 (1966).
 - [3] S. Palmer, P. Dentschuk, and D. Melville, Elastic properties of an iron-rhodium alloy, *physica status solidi (a)* **32**, 503 (1975).
 - [4] F. H. Featherston and J. Neighbours, Elastic constants of tantalum, tungsten, and molybdenum, *Physical Review* **130**, 1324 (1963).
 - [5] M. A. Durand, The temperature variation of the elastic moduli of nacl, kcl and mgo, *Physical Review* **50**, 449 (1936).
 - [6] F. Nix and D. MacNair, The thermal expansion of pure metals. ii: molybdenum, palladium, silver, tantalum, tungsten, platinum, and lead, *Physical Review* **61**, 74 (1942).
 - [7] M. Ibarra and P. Algarabel, Giant volume magnetostriction in the ferh alloy, *Physical Review B* **50**, 4196 (1994).
 - [8] G. White and O. Anderson, Grüneisen parameter of magnesium oxide, *Journal of Applied Physics* **37**, 430 (1966).
 - [9] R. S. Krishnan, R. Srinivasan, and S. Devanarayanan, *Thermal expansion of crystals: international series in the science of the solid state* (Elsevier, 2013).
 - [10] D. Zahn, H. Seiler, Y. W. Windsor, and R. Ernstorfer, Ultrafast lattice dynamics and electron–phonon coupling in platinum extracted with a global fitting approach for time-resolved polycrystalline diffraction data, *Structural Dynamics* **8**, 064301 (2021).
 - [11] Z. Lin, L. V. Zhigilei, and V. Celli, Electron-phonon coupling and electron heat capacity of metals under conditions of strong electron-phonon nonequilibrium, *Physical Review B* **77**, 075133 (2008).

- [12] R. Shayduk, V. Vonk, B. Arndt, D. Franz, J. Stremper, S. Francoual, T. F. Keller, T. Spitzbart, and A. Stierle, Nanosecond laser pulse heating of a platinum surface studied by pump-probe x-ray diffraction, *Applied Physics Letters* **109**, 043107 (2016).
- [13] M. Richardson, D. Melville, and J. Ricodeau, Specific heat measurements on an fe rh alloy, *Physics Letters A* **46**, 153 (1973).
- [14] G. K. White and S. Collocott, Heat capacity of reference materials: Cu and w, *Journal of physical and chemical reference data* **13**, 1251 (1984).
- [15] T. Barron, W. Berg, and J. Morrison, On the heat capacity of crystalline magnesium oxide, *Proceedings of the Royal Society of London. Series A. Mathematical and Physical Sciences* **250**, 70 (1959).
- [16] B. Bergman, G. Ju, J. Hohlfeld, R. J. van de Veerdonk, J.-Y. Kim, X. Wu, D. Weller, and B. Koopmans, Identifying growth mechanisms for laser-induced magnetization in ferh, *Physical Review B* **73**, 060407 (2006).
- [17] A. J. Slifka, B. J. Filla, and J. Phelps, Thermal conductivity of magnesium oxide from absolute, steady-state measurements, *Journal of research of the National Institute of Standards and Technology* **103**, 357 (1998).
- [18] M. Duggin, The thermal conductivities of aluminium and platinum, *Journal of Physics D: Applied Physics* **3**, L21 (1970).
- [19] Y. Chen, J. Ma, and W. Li, Understanding the thermal conductivity and lorentz number in tungsten from first principles, *Physical Review B* **99**, 020305 (2019).
- [20] L.-Y. Chen and D. W. Lynch, Ellipsometric studies of magnetic phase transitions of fe-rh alloys, *Physical Review B* **37**, 10503 (1988).
- [21] M. Mattern, A. von Reppert, S. P. Zeuschner, M. Herzog, J.-E. Pudell, and M. Bargheer, Concepts and use cases for picosecond ultrasonics with x-rays, *Photoacoustics* **31**, 100503 (2023).
- [22] P. Algarabel, M. Ibarra, C. Marquina, A. Del Moral, J. Galibert, M. Iqbal, and S. Askenazy, Giant room-temperature magnetoresistance in the ferh alloy, *Applied physics letters* **66**, 3061 (1995).
- [23] S. O. Mariager, F. Pressacco, G. Ingold, A. Caviezel, E. Möhr-Vorobeva, P. Beaud, S. Johnson, C. Milne, E. Mancini, S. Moyerman, *et al.*, Structural and magnetic dynamics of a laser induced phase transition in ferh, *Physical Review Letters* **108**, 087201 (2012).
- [24] M. Rössle, W. Leitenberger, M. Reinhardt, A. Koç, J. Pudell, C. Kwamen, and M. Bargheer, The time-resolved hard x-ray diffraction endstation kmc-3 xpp at bessy ii, *Journal of Synchrotron Radiation* **28**, 948 (2021).
- [25] D. Schick, A. Bojahr, M. Herzog, C. v. K. Schmising, R. Shayduk, W. Leitenberger, P. Gaal, and M. Bargheer, Normalization schemes for ultrafast x-ray diffraction using a table-top laser-driven plasma source, *Review of Scientific Instruments* **83**, 025104 (2012).
- [26] D. Schick, R. Shayduk, A. Bojahr, M. Herzog, C. v. Korff Schmising, P. Gaal, and M. Bargheer, Ultrafast reciprocal-space mapping with a convergent beam, *Journal of Applied Crystallography* **46**, 1372 (2013).
- [27] G. Li, R. Medapalli, J. Mentink, R. Mikhaylovskiy, T. Blank, S. Patel, A. Zvezdin, T. Rasing, E. Fullerton, and A. Kimel, Ultrafast kinetics of the antiferromagnetic-ferromagnetic phase transition in ferh, *Nature Communications* **13**, 2998 (2022).
- [28] J. Cao, N. T. Nam, S. Inoue, H. Y. Y. Ko, N. N. Phuoc, and T. Suzuki, Magnetization behaviors for ferh single crystal thin films, *Journal of Applied Physics* **103**, 07F501 (2008).